Surface and Interface Analysis

WILEY

SURFACE and INTERFACE ANALYSIS

RESEARCH ARTICLE OPEN ACCESS

Amorphous Hydrogenated Silicon Carbide Interlayers: Chemical, Optical, and Tribological Behavior for Improving Adhesion of Carbon-Based Films to Ferrous Alloy

Vanessa Piroli[1] | Michael Cristian Goldbeck[1] | Jennifer Stefani Weber[1] | Felipe Cemin[2] | Bruna Louise Perotti[1] | Carla Daniela Boeira[1] | Fernando Alvarez[2] | Newton Kiyoshi Fukumasu[3] | Antonio Ricardo Zanatta[4] | Alexandre Fassini Michels[1] | Carlos Alejandro Figueroa[1]

[1]Programa de Pós-Graduação em Engenharia e Ciência dos Materiais (PPGMAT), Universidade de Caxias do Sul (UCS), Caxias do Sul, Brazil | [2]Instituto de Física Gleb Wataghin, Universidade Estadual de Campinas (UNICAMP), Campinas, Brazil | [3]Laboratório de Fenômenos de Superfície (LFS), Escola Politécnica, Universidade de São Paulo, São Paulo, Brazil | [4]Instituto de Física de São Carlos, Universidade de São Paulo (USP), São Carlos, Brazil

Correspondence: Vanessa Piroli (vanessa.piroli2@gmail.com)

Received: 8 April 2025 | **Revised:** 13 October 2025 | **Accepted:** 15 December 2025

Keywords: adhesion | DLC | interface | interlayer | temperature

ABSTRACT

Diamond-like carbon thin films have been gaining attention in the last years due to their unique properties, such as low friction coefficient and high wear resistance. However, the lack of adhesion between DLC coatings and ferrous alloys complicates their wider industrial application. Amorphous hydrogenated silicon carbide (a-SiC_x:H) interlayers can be used as a solution for adhesion issues. Nonetheless, for interlayers produced with tetramethylsilane, deposition temperatures higher than 300°C may degrade the previous heat treatment of the substrate. This work aims to verify the influence of chemical, optical, morphological, and tribological properties in the adhesion of a-C:H/a-SiC_x:H/AISI 4140 steel structures deposited with 0.8 Pa as background pressure and low interlayer deposition temperatures ($T \leq 200$°C). The results showed that both chemical and morphological properties strongly modify the adhesion behavior at low deposition temperatures. The optical absorption edge of the samples takes place in energies around 3.5 (or ~350 nm) and ~1.5 eV (or ~850 nm) for the a-SiC_x:H interlayer (mainly deposited at 150°C) and a-C:H film deposited for 60 min, respectively. When the a-SiC_x:H temperature increased from 85°C to 200°C, the oxygen content at the interfaces and in the interlayer decreased as well as the density of defects observed in the a-C:H surface.

1 | Introduction

Diamond-like carbon (DLC) thin films are amorphous carbon materials composed of a variety of hydrogen content and sp^2/sp^3 ratio [1]. Hydrogenated amorphous carbon (a-C:H) is a type of DLC film with a hydrogen content superior than 50%$_{at}$ and sp^3 fraction inferior to 50% [1, 2]. For the last three decades, these coatings have been widely applied in the automotive, aeronautical, biomedical, and decorative industries due to their low coefficient of friction, high wear resistance, hardness, and chemical inertness [3, 4]. However, when deposited on ferrous alloy, adhesion issues still represent a big obstacle to its widespread application. The adhesion failure on DLC/ferrous alloy is attributed to the lack of chemical affinity between C (DLC) and Fe (alloy) at an interfacial level and to the high levels of internal stress in the coating [5, 6].

In order to minimize adhesion issues, some alternatives can be taken into account, like (1) the introduction of an interlayer (i.e., layer placed between other layers with different compositions), (2) the production of multilayered configurations, and/or (3) the doping of the coating with metallic or nonmetallic elements [7, 8]. The use of metallic interlayers can improve adhesion at interesting levels, such as 74 N for critical scratch

loads when DLC coatings using CrC interlayers are deposited by a reactive magnetron sputtering/plasma enhanced chemical vapor deposition (PECVD) technique [9]. Nevertheless, high-cost, complex hybrid techniques and low background pressures (e.g., 0.005 Pa) are still needed for the deposition of DLC/metallic interlayer/ferrous alloy systems [9, 10]. In this scenario, Si-containing interlayers gain attention for their positive effect on adhesion and the easiness of the deposition with simple low-cost techniques (e.g., PECVD) where less exigent requirements for adhesion are demanded. Moreover, Si has a good chemical affinity with DLC and ferrous alloy main elements ($\Delta H_{formation}$ for Si–C: −318 kJ.mol^{-1} and $\Delta H_{formation}$ for Si–Fe: −73.9 kJ.mol^{-1}) [11, 12].

The Si-containing interlayers can be deposited from organosilanes liquids, such as tetramethylsilane (TMS, $C_4H_{12}Si$), hexamethyldisiloxane (HMDSO, $C_6H_{18}OSi_2$), and tetraethoxysilane (TEOS, $C_8H_{20}O_4Si$), which are safe deposition choices compared with inflammable gases such as silane (SiH_4). However, high deposition temperatures ($T \geq 300°C$) are still demanded to ensure minimum adhesion in deposition systems with high background pressures (~1.5 Pa). It is well known that oxygen damages the adhesion of DLC/Si-containing interlayer/ferrous alloy configurations by bonding with Si, C, and Fe at both interfaces, thus preventing what should have been dangling bonds [13, 14]. By interface, it is understood a region located at the boundary of different materials. The use of high interlayer deposition temperatures enables the desorption of part of this oxygen content. Consequently, stronger bonds will form in both interfaces to ensure the coating's adhesion [13, 15].

Nevertheless, industrial production in high temperatures is somehow unfeasible because of the undesirable changes in the previous heat treatments and dimensional accuracy of the ferrous alloy [15]. The goal of this work is to study the influence of the hydrogenated amorphous silicon carbide (a-SiC$_x$:H) interlayer's deposition temperature (starting at 85°C) using TMS on the adhesion of a-C:H thin films to AISI 4140 steel, considering the effects of chemical, structural, optical, and morphological properties.

2 | Materials and Methods

AISI 4140 steel bars (with wt% of C: 0.38–0.43; Mn: 0.75–1.00; Mo: 0.15–0.25; Cr: 0.80–1.10; Si: 0.15–0.35; P ≤ 0.035; S ≤ 0.04 and Fe in balance) were initially cut into discs with 13 mm of diameter and 5 mm of thickness. The steel discs (~23 HRc) were ground with Si/C abrasive paper no. 220, 320, 500, 800, 1000, and 1200 grits and mirror-polished with a diamond suspension of 3-μm particle size. The mirror-like substrates were stored with oil and cotton to avoid surface oxidation before the thin film's deposition.

Prior to each deposition process, the samples were embedded in acetone and cleaned in ultrasound (for 30 min at 30°C) to remove oil remnants. The a-C:H and a-SiC$_x$:H thin films were deposited by PECVD using a bipolar DC-pulsed source with frequency and pulse fixed at 20 kHz and 20 μs, respectively, and adjustable voltage (0–1000 V) and current (0–4 A). The PECVD technique allows the deposition of a-C:H coatings with high atomic packing and thermal stability in complex geometries [16]. Furthermore, it is a simple and low-cost process, which makes the production of coatings more affordable in the industry. Initially, the samples were positioned above the sample holder. When voltage was applied, the plasma was electrostatically confined through a segmented hollow cathode (SHC) arrangement around the sample holder. Alternated anode and cathode rods were positioned to enable electrical discharges towards the substrate, allowing homogeneous DLC films to be deposited.

At the beginning of the deposition process, the reaction chamber was evacuated to ~0.8 Pa by using a tandem of rotary vane pump and roots blower. This is a cheap mechanical pumping system when compared with turbomolecular pumps. Gas lines were purged to avoid contamination in the system. The deposition of a-C:H and a-SiC$_x$:H thin films followed four steps:

1. After the chamber reached 0.8 Pa, the samples were submitted to an argon plasma etching (Ar, 99.9% purity) for 30 min. The purpose of an Ar sputtering is to remove surface oxides and contaminations on the sample's surface. During this step, the sample holder was gradually heated up to 85°C–300°C, according to each set of samples.
2. Subsequently, the a-SiC$_x$:H interlayer was deposited from the evaporation and ionization of a mixture of TMS (99% purity, Sigma-Aldrich) and Ar for 10 min at −500 V. The sample holder temperature varied from 85°C to 300°C.
3. In Step 3, the sample holder was cooled down until it reached 80°C, which was the temperature applied for the a-C:H film's deposition.
4. The last part consisted of depositing the a-C:H coating from a mixture of Ar and acetylene (C_2H_2, 99.6% purity) for 1 or 60 min, at −800 V.

As stated in Step 4, two sets of samples were produced based on the deposition time of the a-C:H coatings. The first one was composed of samples with 60 min (deposition time) of a-C:H films and the second one of 1 min. The use of 1-min deposition aimed to protect the a-SiC$_x$:H from oxidation and impurities. The three first steps of the methodology were identical in both sets of samples. Table 1 shows all experimental conditions applied to produce the thin films.

Field emission gun scanning electron microscopy (FEG-SEM, Tescan—Mira 3) and energy-dispersive X-ray spectroscopy (EDS) were used for the characterization of the morphology, thickness, and chemical composition (qualitatively) of the a-SiC$_x$:H and a-C:H coatings by cross-section imaging and chemical mapping. EDS employed a silicon drift detector (SDD).

X-ray photoelectron spectroscopy (XPS) was used to identify the chemical bonding and estimate the relative atomic concentrations at both a-C:H/a-SiC$_x$:H and a-SiC$_x$:H/steel interfaces as well as in the a-SiC$_x$:H layer. The analyses were carried out in a Thermo Alpha 110 Hemispherical Analyzer equipment using the nonmonochromatized 1486.6 eV photons from the K_α transition of an aluminum target. The total resolution was 1.2 eV considering both hemispherical analyzer and X-ray line width.

TABLE 1 | Experimental conditions for the deposition of a-SiC_x:H and a-C:H coatings with 1 and 60 min of deposition time. All coatings were deposited in a PECVD equipped with a pulsed DC source of +30 V pulse, duty cycle of 40%, and 10 kHz.

	Samples with 1 min a-C:H			Samples with 60 min a-C:H		
Step	**Ar etching**	**a-SiC_x:H interlayer**	**a-C:H coating**	**Ar etching**	**a-SiC_x:H interlayer**	**a-C:H coating**
Pressure (Pa)	10	25	20	10	25	20
Precursor(s)	Ar	TMS and Ar	C_2H_2 and Ar	Ar	TMS and Ar	C_2H_2 and Ar
Flow rate	30 sccm	4 $g.h^{-1}$ and 40 sccm	15 and 4 sccm	30 sccm	4 $g.h^{-1}$ and 40 sccm	15 and 4 sccm
Bias (V)	−500	−500	−800	−500	−500	−800
Time (min)	30	10	1	30	10	60
Temperature (°C)	~25	85, 100, 125, 150, 175, 200, 250, 300	80	~25	85, 100, 125, 150, 175, 200, 250, 300	80

The binding energy associated with the $3d_{5/2}$ electrons of silver, located at 368.2 ± 0.1 eV, was used to calibrate the binding energy scale. Ag was also used to determine the work function of the analyzer. To reduce sample charging, the metallic samples were fixed in a stainless-steel holder using stainless-steel clips. All narrow XPS spectra were energy-corrected by the Ar 2p3/2 spectral component at 242 eV because Ar-implanted ions are present after each cleaning [17]. Adventitious carbon was not used for calibration, because it is not reliable and may lead to unphysical results and vary in a wide range, as recently shown in other studies [18–20]. The samples with 1 min of a-C:H deposition were used for XPS analyses. The measurement procedure consisted of two main steps. Initially, the samples were inserted in an ion beam-assisted deposition (IBAD) chamber with the aim of applying an Ar^+ ion etching on the surface of the thin film. The Ar^+ ions were generated by a 1″ diameter Kaufman cell at 400 eV, and the current density on the sample surface was 0.18 $mA.cm^{-2}$. Secondly, the samples were transferred to an ultrahigh vacuum (UHV) chamber (with average working pressure ~8E-7 Pa) to be irradiated by an X-ray beam. This whole procedure was repeated until the outermost interface was reached, which happened when a peak located in the binding energy of Si 2p photoelectrons first appeared. The average sputtering time to reach the a-C:H/a-SiC_x:H interface, the a-SiC_x:H layer and the a-SiC_x:H/steel interface were 1, ~10, and ~25 min, respectively. Thermo Advantage software was used to perform the deconvolution of the peaks in the XPS spectra and to determine the bands associated with each type of photoemitted electron. Moreover, the background signal was subtracted from the Shirley model to correct the inelastic scattering signal of the electrons [21]. The atomic relative concentration was obtained using the appropriate sensitivity correction factors given by Wagner et al. [22].

Fourier transform infrared spectroscopy (FTIR, PerkinElmer, Spectrum 400) qualitatively characterized certain chemical bonds in the Si-containing interlayer and in the a-C:H coating. This characterization technique is based on the interaction between the IR beam and matter. Such interaction induces energy absorption and vibrations of specific chemical bonds [23]. In all FTIR spectra, the background was excluded to avoid the presence of humidity peaks as contaminants. Samples with 1 and 60 min of a-C:H deposition were used for the FTIR analysis of a-SiC_x:H and a-C:H, respectively.

The chemical structure of the a-C:H thin films was characterized by Raman scattering spectroscopy (Horiba, LabRAM HR Evolution) with a 633 nm laser. In Raman spectroscopy, matter interacts with monochromatic light. The information obtained by the end of the analysis results from the inelastic scattering of the light, which, as in FTIR spectroscopy, can be related to the sample's vibrational states [24].

Optical reflectance (%*R*) measurements of the a-C:H/a-SiC_x:H samples were carried out in the 215- 1050 nm wavelength range by means of a portable spectrometer (Ocean Optics HR4000), a deuterium-halogen light source, and special optical fibers. The sample measured areas stayed around 3 mm^2, and all spectra were corrected by the optical response of the system to ensure 100% light reflection from a specular reflectance standard.

Chemical depth profiles were obtained by glow discharge optical emission spectroscopy (GDOES, Horiba GD—Profiler 2). In GDOES spectroscopy, Ar atoms are accelerated (by using a DC voltage) towards the sample's surface. The impact between Ar atoms and the surface generates sputtered atoms, which are accelerated towards the anode. Subsequently, there is a collision between Ar atoms, excited sample atoms, and electrons. This phenomenon results in the emission of photons with characteristic wavelengths that are detected by photo sensors, thus originating GDOES spectra [25].

The adhesion of the coatings was quantitatively evaluated by two techniques: (1) nanoscratch test and (2) scratch test. The nanoscratch test was applied to identify "Lc_1" (start of plastic deformation at the coating), whereas the scratch test focused on obtaining "Lc_2" (critical scratch load, corresponding to the beginning of the coating's delamination). The nanoscratch test was performed using a Nano Test 600 system (Micro Materials Ltd). This method involves scratching the film with a conical diamond tip of 25-μm radius while applying a progressively increasing normal load up to 500 mN. The loading rate was set at 0.15 $mN.s^{-1}$, and the track length was 1800 μm. For each sample, five tracks were produced. Lc_1 was estimated as the average value obtained from these five tracks. Optical microscopy (microscope Zeiss, AxioScope 5) was employed for the observation of the nanoscratch trails. The scratch test (Bruker, UMT 2) allowed to determine adhesion features as well as failure modes and damage mechanisms. In this technique,

three scratch trails of 3 mm each were made by a Rockwell C tip with a radius of 200 μm. The scratch parameters were a ramping load from 0 to 10 N (maximum normal load) applied during 180 s [15]. The scratch trails were characterized by FEG-SEM (analysis of the failure point of the a-C:H coatings) and EDS (chemical mapping to identify the failure interface—outermost or innermost).

The hardness and friction coefficient of the a-C:H coatings were measured in a nanotribometer (Micro Material, NanoTest-600) using a Berkovich indenter and a conical diamond tip (25 μm radius), respectively. In terms of hardness, the Berkovich tip was indented at 0.1 mN up to a maximum depth of 10% of the coating's thickness. Hardness was measured with a constant load rate of 0.1 mN.s^{-1}. Regarding the friction coefficient, the conical diamond tip slid unidirectionally (for 10 times) on the sample's surface, using a constant normal force of 10 mN and loading rate of 0.01 μm.s^{-1}.

Optical microscopy was applied for the analysis of the surface morphology of the coatings. Five micrographs with 100× magnification (microscope Zeiss, AxioScope 5) were treated with *ImageJ* software in order to determine the number of defects per square centimeter (i.e., the density of defects) on the coating's substrate. The roughness of the a-C:H coatings was evaluated using profilometry (Taylor Hobson, Intra TalySurf profilometer). Five measurements were taken on each surface considering a test field equal to 7 mm.

3 | Results and Discussion

3.1 | Structural and Optical Properties of a-SiC$_x$:H Interlayers and a-C:H Films

The carbonaceous coatings were characterized by Raman spectroscopy. Figure 1 shows the Raman spectrum of the coating with the interlayer deposited at 175°C. This spectrum determines that the coating is a typical hydrogenated amorphous carbon and it is representative of the entire set of samples. The spectrum was deconvolved into two characteristic bands of the hydrogenated carbon films. Both D and G-bands correspond to the chemical bonds between the sp^2-type carbons. More specifically, the D-band (disorder), centered at ~1312 cm^{-1}, represents the breathing mode of sp^2 carbon atoms in the rings while the G-band (graphite), centered at ~1511 cm^{-1}, characterizes the stretching of all pairs of sp^2 atoms in both aromatic rings and chain structures. In addition, the position of the G-band was shifted to a lower wavenumber if compared with the positions found by Tamor and Vassell (i.e., ~1550 cm^{-1}) [26].

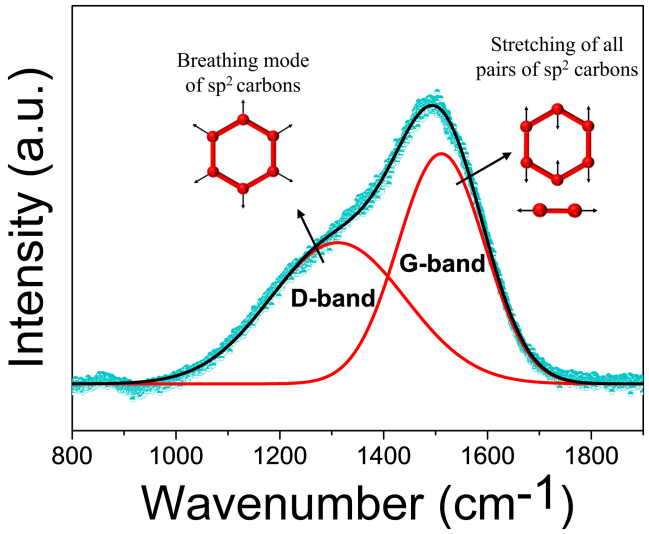

FIGURE 1 | Raman spectrum of the a-C:H coating for the sample with the interlayer deposited at 175°C, evidencing two deconvoluted bands, and illustration of the C=C vibration modes.

The presence of functional groups in the a-C:H coating and a-SiC$_x$:H interlayers was evaluated by attenuated total reflection FTIR spectroscopy. Figure 2a shows the FTIR analysis for the a-C:H coatings according to the interlayer's deposition temperature. As it can be seen, the position of the peaks is not so clear between 650 and 1000 cm^{-1}, probably because there is a mix of a-C:H and Si–C contributions inside the hydrogenated coating, which could be due to residuals from the interlayer. It is possible to observe (1) a contribution at ~914 cm^{-1}, attributed to sp^2 CH_2 (olefinic) group; (2) a small contribution at ~1515 cm^{-1} related to a coexistence of sp^2–sp^3 C–C vibration modes; (3) a considerable peak at ~1720 cm^{-1}, which represents the vibration of the C=O bond; and (4) a peak at ~3680 cm^{-1} corresponding to the O–H stretching vibration [28, 29]. The C=O and O–H contributions appeared only for the sample with a-SiC$_x$:H interlayer deposited at 150°C. These peaks were not expected and can be interpreted as a contamination in the a-C:H coating during the deposition process.

Regarding the a-SiC$_x$:H interlayer (Figure 2b), five distinguished contributions were observed: Si–$(CH_3)_3$ stretching mode at ~830 cm^{-1}/C–H_n wagging mode in Si–CH_3 at ~830 cm^{-1}, Si–O–Si stretching mode at ~1000 cm^{-1}, C=C stretching mode at ~1560 cm^{-1}, Si–H_n stretching mode at ~2100 cm^{-1}, and C–H_n stretching mode at ~2900 cm^{-1} [30–32]. The Si–$(CH_3)_3$ stretching peak was more intense than the Si–O–Si peak for all the analyzed conditions. Such a result indicated the presence of more oxygen-free bonds in the Si-containing interlayer. In addition, one can observe a slight decrease in the intensity of the Si–H_n peak when the temperature increases from 85°C to 300°C due to Si and H desorption at high deposition temperatures. Figure 2c exhibits the comparison of the FTIR spectra for the a-SiC$_x$:H interlayer for the samples deposited with a background pressure of 0.8 (this work) and 1.5 Pa [13, 27]. The data were not normalized, in accordance with Cemin et al. [27]. Regarding the deposition at 100°C, the samples with a background pressure of 1.5 Pa showed more intense oxygen-containing peaks than Si and C-containing ones. For 0.8 Pa, this behavior changed. Moreover, the Si–$(CH_3)_3$ stretching peak was more intense than the Si–O–Si peak for both background pressures, at higher temperatures (e.g., 300°C). The reduction of the Si–O–Si peak corroborates the results found by XPS about the decrease in oxygen percentage and the increase in the structure's adhesion with the decrease of the background pressure as will be shown later. The word structure refers to the a-C:H/a-SiC$_x$:H/steel multilayered configuration.

Most of these results are consistent with the optical behavior of the a-C:H/a-SiC$_x$:H samples involving different deposition

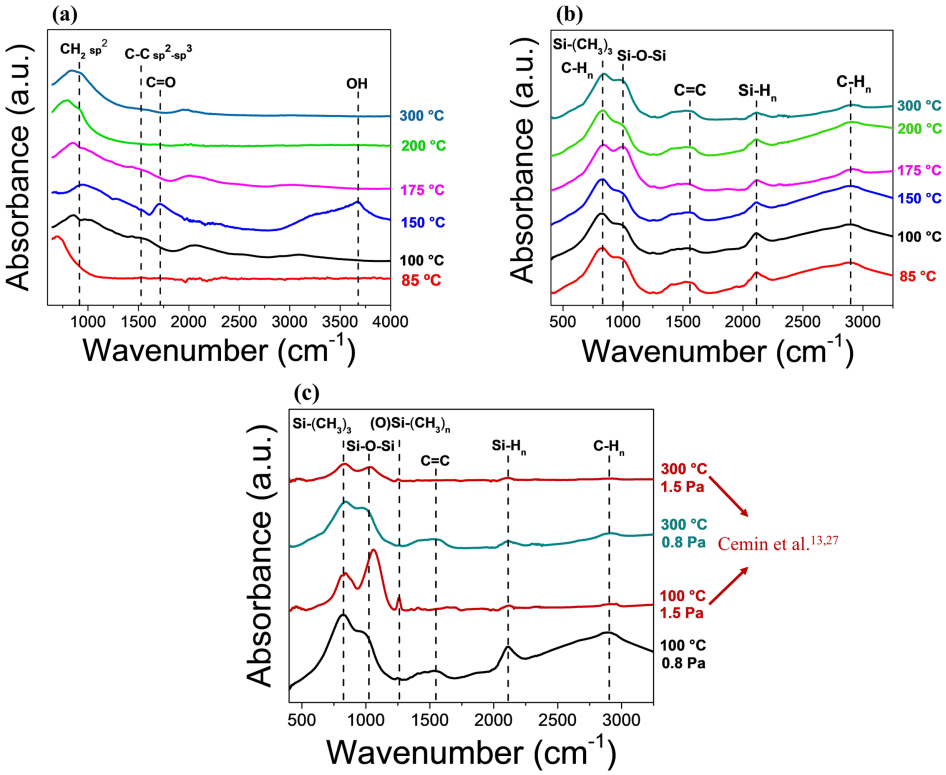

FIGURE 2 | FTIR spectra of the (a) a-C:H coatings and (b) a-SIC$_x$:H interlayers with variation of the deposition temperature (normalized data) and (c) comparison of a-SiC$_x$:H interlayer FTIR spectra for samples deposited with a background pressure of 0.8 and 1.5 Pa (non-normalized data) [13, 27].

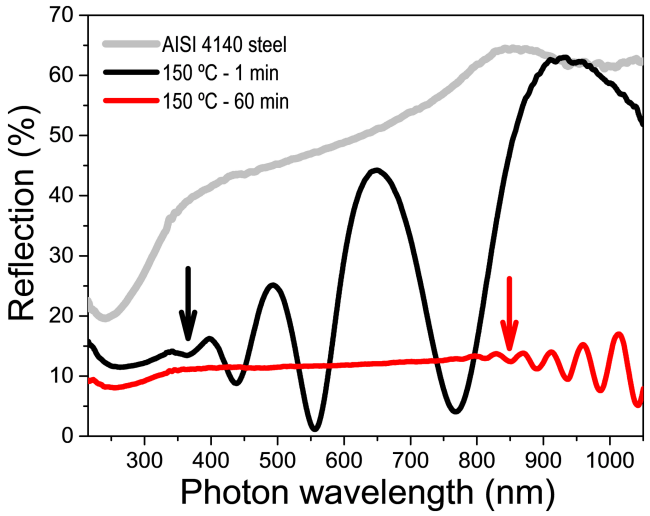

FIGURE 3 | Optical reflectance spectra of the a-C:H/a-SiC$_x$:H samples deposited at 150°C (1 and 60 min deposition time), along with the spectrum of the bare steel substrate. The downward arrows indicate the position where the optical absorption edges of the samples are expected to occur.

temperatures and times (i.e., 1 and 60 min). Figure 3 shows a typical example of the optical reflectance spectra—this time, considering the sample with the a-SiC$_x$:H interlayer grown at 150°C (further spectra can be seen in Figure S1). According to Figure 3, it is clear the difference between the optical reflectance of the bare substrate (steel) and those presented by the samples that are characterized by the presence of some fringe patterns that occur because of light interference effects at the air/a-C:H/a-SiC$_x$:H/steel interfaces. Both the wavelength and amplitude of these interference patterns are correlated with the thickness and index of refraction n of the films [33]. In the first case, the wavelength of the fringes confirms the fact that longer deposition times produced thicker a-C:H films (i.e., more interference fringes). Regarding the amplitude of the fringes, the results indicate that the interference phenomena occur mainly at the air/a-C:H interface ($n_{air} \sim 1$ vs. $n_{a\text{-}C:H} \sim 2$) for the thicker film, whereas the opposite takes place with the thinner one ($n_{air} \sim 1$ vs. $n_{a\text{-}SiC:H} \sim 3$) [34]. The most important feature of Figure 3, however, refers to the energy at which the optical absorption edge of the samples takes place, that is, around 3.5 (or ~350 nm) and ~1.5 eV (or ~850 nm) for the a-SiC$_x$:H interlayer mainly (deposited at 150°C plus a-C:H film deposited during 1 min) and a-C:H film deposited for 60 min, respectively. These values can be considered to estimate the average optical bandgap E_{gap} of the a-C:H/a-SiC$_x$:H samples that, in spite of some experimental limitations (e.g., like the absence of transmission measurements), are in accord with the Raman measurements. More specifically, based on the position of the G-band, the E_{gap} of the present samples are expected to occur at approximately 1.5 and above ~2.5 eV for the a-C:H films deposited for 1 and 60 min, respectively [26]. Figure S1 displays the optical reflectance spectra of the samples with different a-SiC$_x$:H deposition temperatures and a-C:H deposition time of (a) 1 and (b) 60 min.

3.2 | Morphology and Chemical Structure of a-SiC$_x$:H Interlayers and a-C:H Films

Three different regions were spotted on the cross-section image by FEG-SEM for all samples. Figure 4a shows the case

of a sample with the interlayer deposited at 200°C. The top, middle, and lower regions correspond to the a-C:H coating, the a-SiC_x:H interlayer, and the AISI 4140 steel, respectively. The a-C:H and a-SiC_x:H thin films displayed amorphous morphology. The interlayer's thickness ranged from ~380 (for 100°C) to ~170 nm (for 300°C). The average thickness of the a-C:H coating was (3.20 ± 0.02) μm [15]. The EDS of a similar region, exhibited in Figure 4b, showed the C, Si, Fe, and O chemical maps for the multilayered configuration. It was possible to observe that carbon was more visible on the top layer (a-C:H), whereas silicon and iron were mainly present in the intermediate (a-SiC_x:H) and bottom layers (steel), respectively. Oxygen (O) was detected specially in the steel substrate, probably as oxides.

The chemical structure at the a-C:H/a-SiC_x:H (outermost) interface in terms of type of chemical bonds and environment was determined by XPS. Figure 5 contains a schematic of the region analyzed by XPS.

Figure 6a,b shows the X-ray photoemission spectra related to the C 1s and Si 2p core electron levels, respectively, for the samples with the interlayers deposited at 85°C, 150°C, and 200°C. Three contributions were revealed through the proposed deconvolution of the band associated with the C 1s photoelectrons (Figure 6a): Si–C, C–C, and C–O(–H), with respective binding energies of ~283.5, ~284.5, and ~286.5 eV [17, 27, 35]. It is worth noting that the region analyzed by XPS included the a-C:H thin film and the first atomic layers of the a-SiC_x:H interlayer. Thereby, a more significant C–C contribution appeared in the C 1s spectrum. The proposed deconvolution of the band associated with the Si 2p photoelectrons (Figure 6b) exhibited two main contributions: Si–C (at ~100.5 eV) and O–Si–C (at ~101.7 eV) [17, 27, 35]. It was possible to notice a reduction in the O–Si–C peak intensity when the interlayer's deposition temperature increased from 85°C to 200°C. Proportionally, there was a slight increase in the Si–C peak intensity.

Figure 6c,d exhibits the evolution of the amount of chemical bonds at the outermost interface as a function of the interlayer's deposition temperature for carbon and silicon atoms, respectively. The chemical bond percentages were estimated by integrating the areas under the C 1s and Si 2p deconvoluted bands. In the case of carbon chemical bonds, there is a slight reduction of the C–O(–H) atomic content with the increase in the a-SiC_x:H deposition temperature. Furthermore, the C–Si atomic content decreased from the sample 150°C to 200°C. In the case of silicon chemical bonds, there is a proportional reduction of the O–Si–C bonds with the increase in Si–C bonds when the interlayer's deposition temperature varied from 85°C to 200°C.

The spontaneity of a chemical reaction can be predicted by thermodynamics in equilibrium conditions. For example, the Gibbs free energy of formation (ΔG_f) is a thermodynamic parameter that assumes negative values when a chemical reaction is spontaneous and product favored. It is important to point out that ΔG_f can vary with temperature, pressure, and concentration of the reactants [36]. The decrease of C–O(–H) bond content (Figure 6c) with the increase in the interlayer's deposition temperature can be associated with the thermal desorption of oxygen as light chemical species. When desorbed at high temperatures (e.g., 200°C), oxygen is thermodynamically preferred to form volatile compounds, such as $H_2O_{(g)}$ ($\Delta G_f = \sim -220.4\ kJ.mol^{-1}$), $CO_{2(g)}$ ($\Delta G_f = \sim -394.8\ kJ.mol^{-1}$), $SiO_{(g)}$ ($\Delta G_f = \sim -142.8\ kJ.mol^{-1}$), and $O_{2(g)}$ [36]. Furthermore,

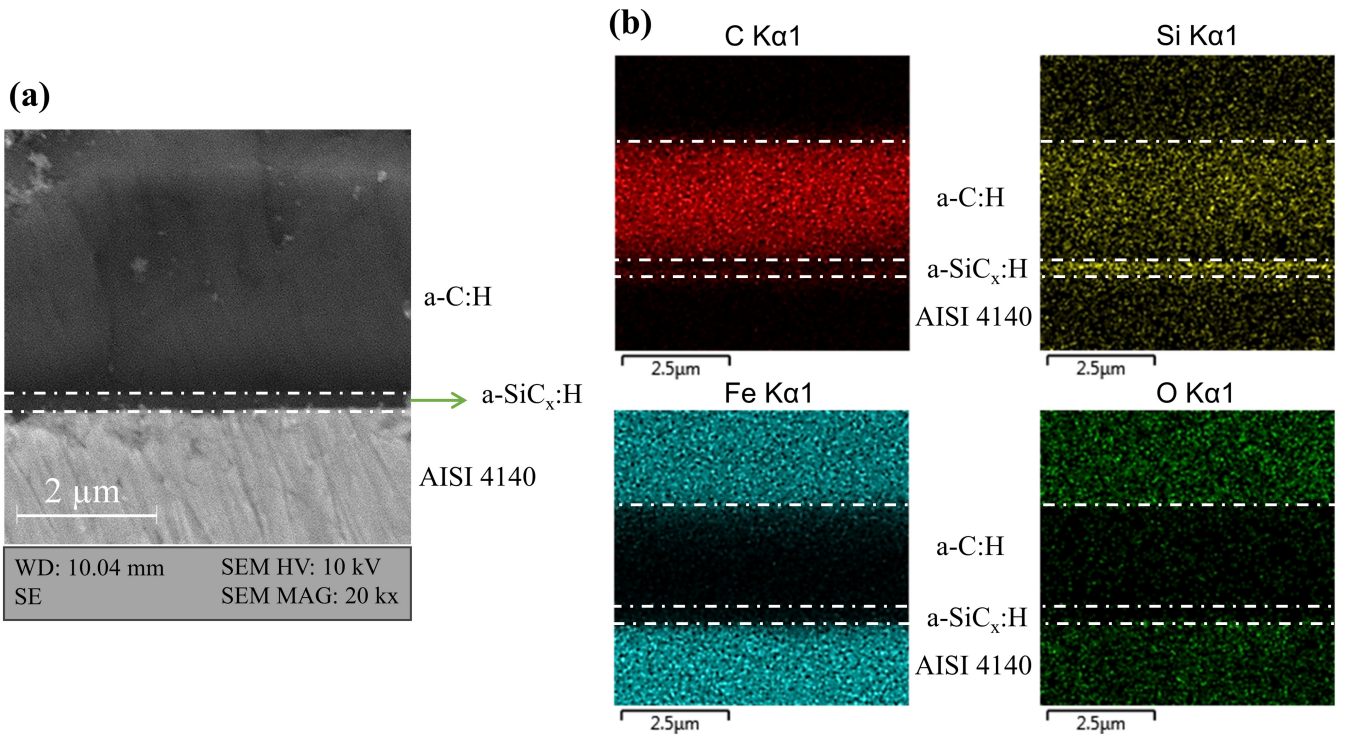

FIGURE 4 | (a) Cross-section FEG-SEM micrograph of the sample with interlayer deposited at 200°C, displaying the steel substrate, a-SiC_x:H, and a-C:H thin films. (b) Chemical mapping by EDS of a similar region. The dashed lines are only tools for better delimitation of the layers.

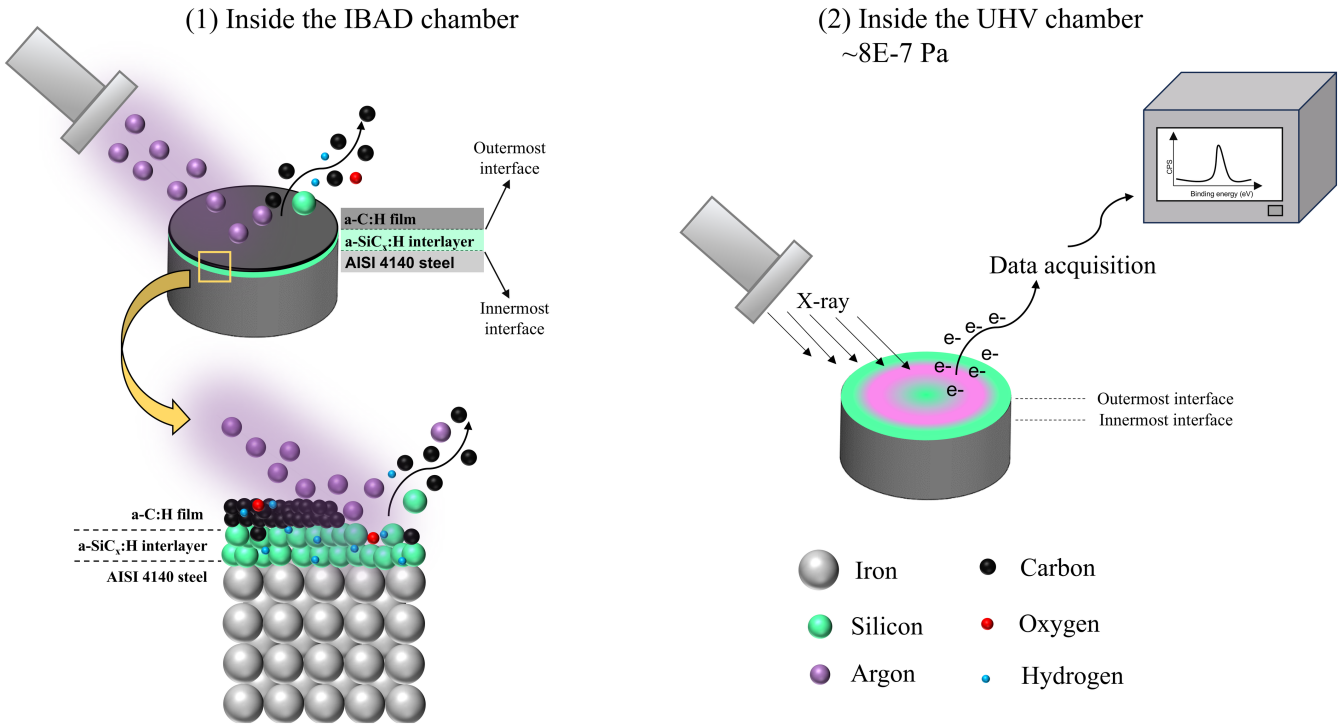

FIGURE 5 | Schematics of the XPS analysis at the outermost region of the a-C:H/a-SiC$_x$:H/ferrous alloy structure.

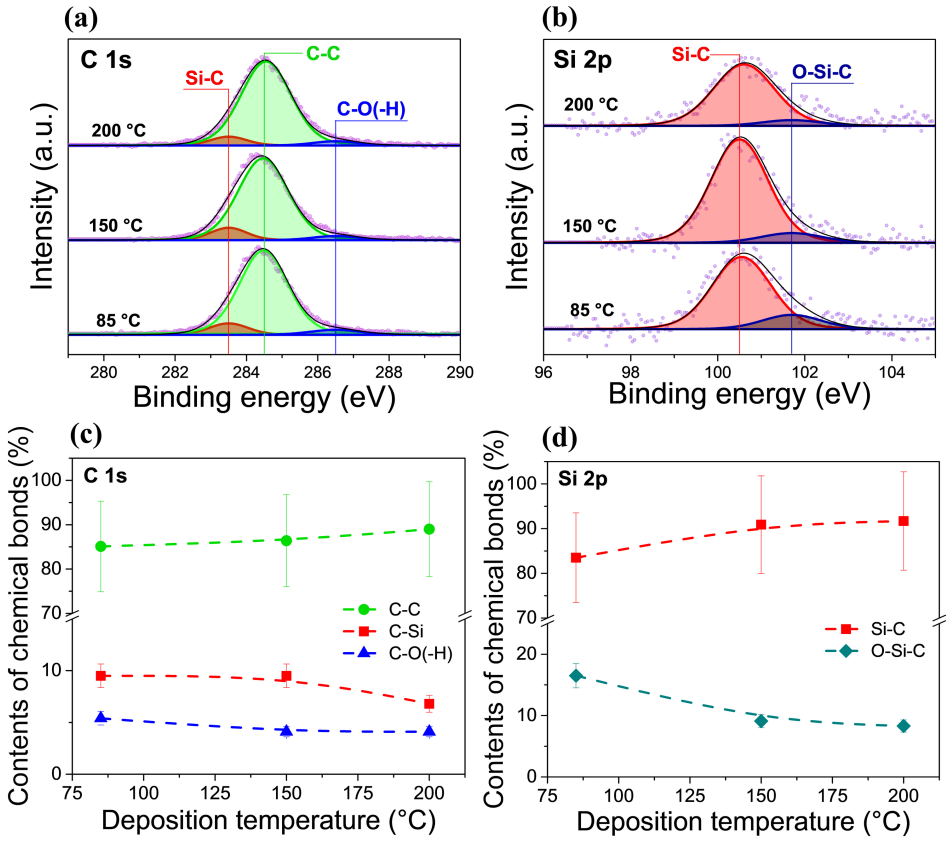

FIGURE 6 | XPS bands associated with the (a) C 1s and (b) Si 2p core electron levels for the outermost interface. Estimated contents of chemical bonds measured for (c) carbon and (d) silicon atoms.

the decrease in Si–C bond content when the a-SiC_x:H deposition temperature increased from 150°C to 200°C can also be related to the desorption process of Si as SiO_x compounds. The remaining carbon atoms bind to other carbons, thus leading to an increase in C–C bonds. These carbonaceous bonds are stronger than Si–C, which can justify the improvement of the a-C:H/a-SiC_x:H/steel structure's adhesion at higher temperatures, as it will be further explained.

Regarding the Si 2p spectra (Figure 6b), the increase observed in the Si–C bond content when the temperature ranged from 85°C to 200°C is a consequence of the O–Si–C bond break and oxygen desorption phenomena. The Si–C bonds promote better chemical cohesion at the outermost interface when compared with O–Si–C bonds [15]. Moreover, Cemin et al. [27] explained the thermodynamic non-possibility of Si–O and Si–C chemical transitions by comparing both ΔG_f parameters. Thus, the oxygen desorption explanation is supported. It is important to emphasize that the deconvolution of the bands associated with the C 1s and Si 2p binding energy levels agrees with each other. When the Si-containing interlayer's temperature increases, more C–C and Si–C bonds form at the a-C:H/a-SiC_x:H interface. Such chemical bonds are responsible for maintaining chemical and interfacial adhesion.

Cemin et al. [27] determined by using XPS the main chemical contributions at the a-C:H/a-SiC_x:H interface for samples with the a-SiC_x:H interlayer deposited at 100°C and 500°C with TMS and background pressure of 1.5 Pa. By evaluating the C 1s spectrum, the researchers observed a reduction in C–O(–H) and O–C–O bonds and an increase in C–C and C–Si bonds when temperature increased from 100°C to 500°C. In the Si 2p spectrum, SiO_x and O–Si–C bonds' contributions were more pronounced at lower deposition temperatures. The shift of the Si 2p band at 100°C to higher binding energies indicated a greater presence of SiO_x bonds [27]. The physicochemical properties of the a-C:H/a-SiC_x:H/steel structure, with the interlayers formed by HMDSO at 150°C and with bias variation were investigated by Crespi et al. [30]. While the increase in temperature enhanced the probability of the formation of more C–C bonds and fewer C–Si and C–O(–H) bonds, the increase in bias favored the appearance of more C–Si and fewer C–C and C–O bonds. In the same condition (150°C and −500 V) for both TMS and HMDSO, the atomic contents of ~(90% Si–C/10% O–Si–C) were found for the sample deposited with TMS and ~(30% Si–C/62% O–Si–C/8% Si–O) for the sample produced with HMDSO. Nehate et al. [37] deposited amorphous hydrogenated boron carbide films on silicon with radio-frequency sputtering by varying the substrate temperature between 100°C and 300°C. The C 1s spectra showed a dominating contribution at 284.8 eV related to sp^2 C–C and C–H bonds. At higher substrate temperatures, more C–C bonds were formed. A shoulder peak at 286.4 eV was related to C–O–H and C–O–C bonds. Furthermore, Nishikawa et al. [38] discovered that by incorporating Si atoms in a-C:H films, there was a shift of the Si–C peak to ~284.3 eV in the C 1s spectrum and to ~100.5 eV in the Si 2p spectrum. For a-SiC:H films deposited by PECVD at $T \geq 325$°C, only a peak centered at ~100.2 eV, attributed to Si–C bonds, was found in the Si 2p spectrum. At lower temperatures, Si–O–C contributions (~100.8 eV) started to appear [39].

Figure 7a shows the photoemission spectra related to the O 1s core electron level at the outermost interface for the samples with the interlayers deposited at 85°C, 150°C, and 200°C. Three main contributions were found: O–C (at ~531.5 eV), SiO_x (at ~532.1 eV), with $x < 2$, and Si–O–Si (at ~533 eV) [39, 40]. The overall O 1s band intensity considerably decreased by increasing the deposition temperature. Moreover, considering the proposed deconvolution, the O–C peak intensity reduced with temperature while the Si–O–Si increased. Figure 7b exhibits the evolution of oxygen chemical environment for O–C, SiO_x, and Si–O–Si bonds as a function of the deposition temperature. It was possible to verify a ~70% reduction of O–C bonds and a ~290% increase of Si–O–Si bonds when the temperature ranged from 85°C to 200°C. These shifts in bond percentages could be explained by two thermodynamic parameters: the bond dissociation enthalpy ($\Delta H_{dissociation}$) and the Gibbs free energy of formation (ΔG_f). The $\Delta H_{dissociation}$ is equal to 357.7 kJ.mol^{-1} for the O–C bond and 452 kJ.mol^{-1} for the O–Si bond [11]. A smaller bond dissociation enthalpy indicates that less energy is required for the dissociation (i.e., breaking) of the chemical bonds. Therefore, it is easier to break an O–C

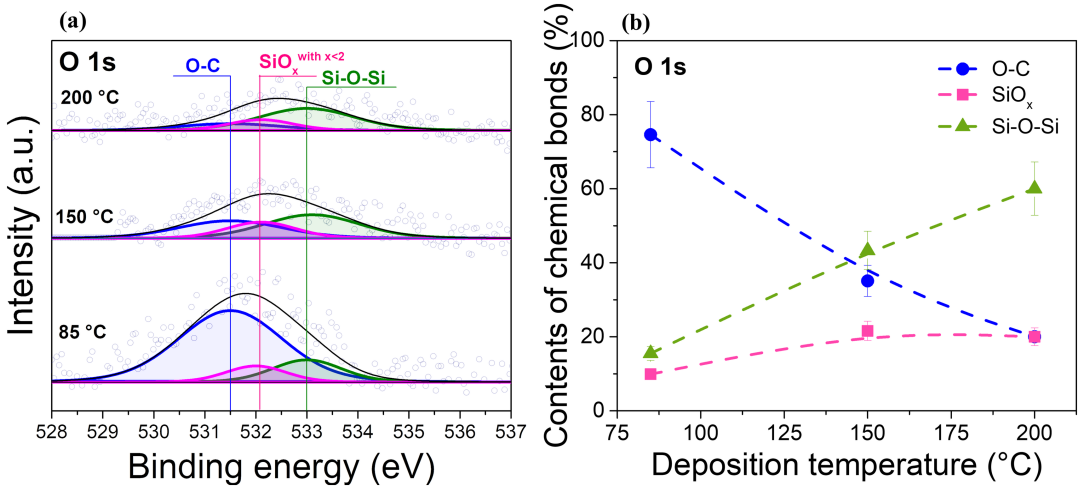

FIGURE 7 | (a) XPS band associated with the O 1s core electron level for the outermost interface and (b) estimated contents of chemical bonds measured for oxygen atoms.

bond in comparison to an O–Si bond when the temperature increases. This fact could justify the relative decrease in O–C atomic content and the relative increase in Si–O–Si and SiO_x bonds. The Gibbs free energy of formation can explain the preferential formation (after desorption) of $CO_{2(g)}$ and $CO_{(g)}$ compounds over $SiO_{(g)}$ ones. The ΔG_f for $CO_{2(g)}$, $CO_{(g)}$, and $SiO_{(g)}$ at 200°C are equal to −394.8, −153, and −142.8 kJ.mol^{-1}, respectively [36]. The more negative ΔG_f, the greater the spontaneity of a reaction. Thus, after thermal desorption, C-containing chemical species have a bigger probability of formation rather than Si-containing species, which reinforces the explanation regarding the variation of the bond contents with the increase in temperature.

The atomic content of oxygen measured by XPS at the a-C:H/a-SiC_x:H (outermost) interface, in the a-SiC_x:H interlayer and at the a-SiC_x:H/steel (innermost) interface is displayed in Figure 8. The innermost interface exhibited the highest atomic content of oxygen (~5%) of the a-C:H/a-SiC_x:H/steel structure. This can be related to the iron oxidation tendency, with the formation of $Fe_3O_{4(s)}$ ($\Delta G_f = -955.9$ kJ.mol^{-1} at 200°C), $Fe_2O_{3(s)}$ ($\Delta G_f = -694.9$ kJ.mol^{-1} at 200°C), and $FeO_{(s)}$ ($\Delta G_f = -239.8$ kJ.mol^{-1} at 200°C) [36]. In the interlayer, the oxygen content varied between 3% and 4%. The outermost interface showed the lowest atomic content of oxygen in the structure. By increasing the a-SiC_x:H deposition temperature, it was possible to observe a decrease in the oxygen content ranging from ~1.5% (at 85°C) to ~0.5% (at 200°C). It is important to emphasize that the oxygen contents were an approximation since the values were measured almost at the lower limit of the XPS equipment. The lower atomic content of oxygen found at 200°C is related to oxygen desorption at elevated temperatures.

Cemin et al. [27] measured ~15%, ~10%, and ~5% as oxygen contents for the samples with the interlayers deposited at 100°C, 300°C, and 500°C, respectively. For the same deposition condition ($T = 100$°C), the sample with a background pressure of 0.8 Pa (this work) presented an oxygen content five times lower than the one with 1.5 Pa

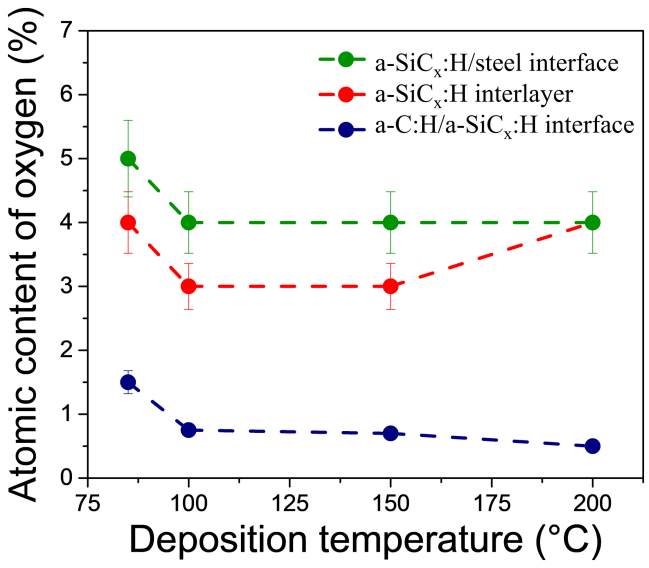

FIGURE 8 | Variation of the atomic content of oxygen present at the interfaces and in the interlayer.

[27]. The samples with the a-SiC_x:H layer deposited at 85°C (0.8 Pa) and 500°C (1.5 Pa) showed similar oxygen contents (~5%). These differences are related to the background pressure of 0.8 Pa, which is ~50% smaller than 1.5 Pa. The lower the background pressure, the longer the mean free paths (λ), the higher the ultimate energy of the ions, and the more energetic the impact of the ions on the sample's surface. Oxygen is then removed from the interlayer and from the interfaces by sputtering and/or thermal desorption [15]. Crespi et al. [30] measured a ~19% oxygen content for the sample with the Si-containing interlayer deposited with HMDSO (−500 V and 150°C) at the outermost interface. The Si precursor HMDSO ($C_6H_{18}OSi_2$) has an oxygen atom in its chemical structure, which is more complicated to be eliminated than an oxygen atom incorporated through impurities confined in the deposition chamber. Moreover, a-SiC_x:H films deposited by PECVD at 200°C (with CH_4 and SiH_4 as precursors) exhibited 10%–13% oxygen when the radio-frequency power varied from 100 to 180 W [41]. Finally, Kwon et al. [42] prepared a-SiC:H films using a mixture of Si_2H_6 and CH_4 at 550°C in a PECVD system with a background pressure of 1.33 Pa. The oxygen content varied between 4% and 7% when the plasma power ranged from 100 to 1600 W.

The in-depth chemical profiles by GDOES as a function of the interlayer's deposition temperature allowed a deeper understanding of the chemistry of the a-C:H/a-SiC_x:H/steel structure. Regarding the oxygen profiles (Figure 9a), one can see a greater oxygen signal on the surface and at the first atomic layers of the a-C:H thin film for temperatures below 125°C. Furthermore, some of the samples deposited with $T \leq 150$°C exhibited a small intensity peak in the O signal at the interlayer region, which indicated an oxygen increase. The silicon profiles (Figure 9b) displayed a single peak across the entire GDOES signal, corresponding to the a-SiC_x:H interlayer. The increase in the deposition temperature (from 100°C to 200°C) was accompanied by a reduction in the full width at half maximum (FWHM) and the intensity of the peaks. Such phenomena can be related to Si thermal desorption at high temperatures. This reduction trend did not apply to the 85°C sample. As explained by Piroli et al. [15], volatile compounds can be released from the interlayer during the a-C:H film deposition due to the similarity of the temperatures (85°C–80°C) at both deposition steps. The carbon profiles (Figure 9c) followed the same trends as the Si ones, evidencing the C thermal desorption at high temperatures. Finally, peak shifts in the C and Si signals were observed towards shorter times. Thus, to reach the interlayer, shorter times were needed at the sputtering of the coatings. The differences in the position of the peaks may be due to (1) the irregularity in the thickness of the a-C:H films and/or (2) the variation in the thickness of the a-SiC_x:H layer. The GDOES analysis corroborated the results found by XPS for samples with a-C:H films deposited with 1 min.

3.3 | Density of Defects and Tribological Properties of a-C:H Films

The a-C:H coatings exhibited average hardness of 17.3 ± 0.7 GPa. A small variation in hardness was observed due to the differences in the surface density of defects as will be shown below. In addition, the mean coefficient of friction was 0.06 ± 0.01, which is consistent with this type of material.

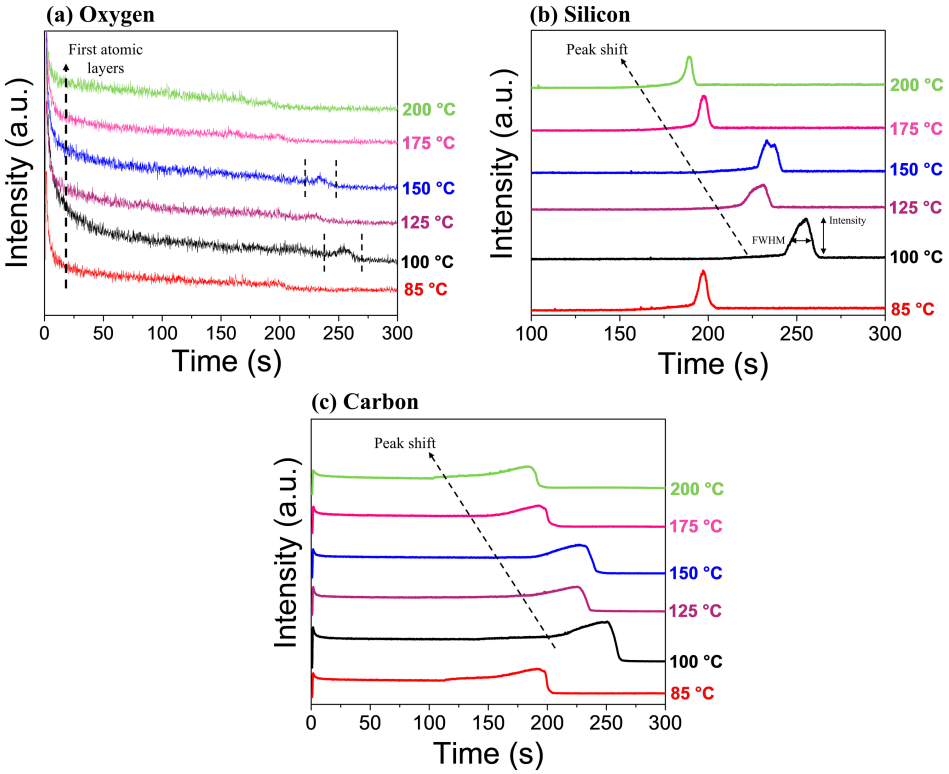

FIGURE 9 | In-depth chemical profiles displaying (a) oxygen, (b) silicon, and (c) carbon signals as a function of the interlayer deposition temperatures. The dashed lines and the arrows are only tools for better visualization of the phenomena.

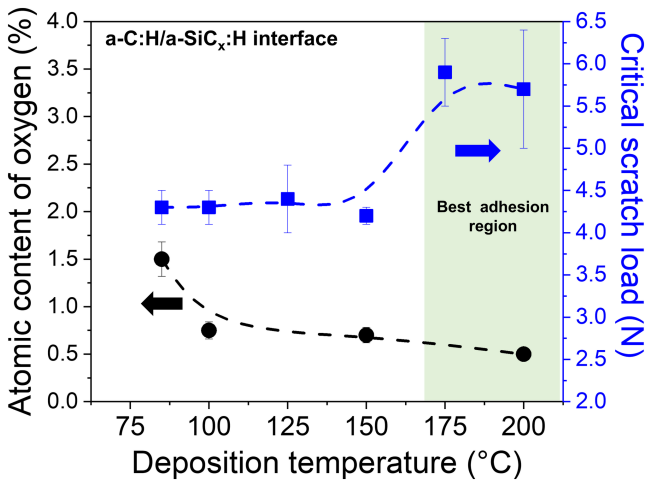

FIGURE 10 | Variation of the atomic content of oxygen and critical scratch load with a-SiC$_x$:H deposition temperature at the outermost interface.

Oxygen content is a crucial aspect to determine the adhesion of a-C:H thin films to metallic substrates. Past researches have stated that the delamination of a-C:H coatings usually occurred at the outermost interface of the system, which comprehended the a-SiC$_x$:H interlayer and the a-C:H film [30, 43]. Figure 10 shows the relation between the oxygen content at the outermost interface and the critical load of a-C:H thin films as a function of the interlayer's deposition temperatures. All deposition conditions showed completely adhered films to AISI 4140 steel [15]. Critical loads ranged from ~4 to 6 N for all deposited films. The atomic content of oxygen and the critical loads exhibited inverse behavior with temperature. By increasing the interlayer's deposition temperature from 85°C to 200°C, one can observe a gradual reduction in oxygen content at the a-C:H/a-SiC$_x$:H interface and an improvement in the critical load of the films. The two best adhesion conditions were observed for 175°C and 200°C, which exhibited the highest values of Lc$_2$ and the lowest oxygen content at the outermost interface. This result suggests the possibility of a wider industrial application of a-C:H thin films in relatively low-cost deposition processes, such as PECVD with simple mechanical pumping.

For comparison reasons, a-C:H thin films produced with similar deposition conditions and at higher background pressure (i.e., 1.5 Pa) showed complete adhesion for the a-SiC$_x$:H interlayer deposited with a minimum temperature of 300°C. This condition exhibited Lc$_2$ of ~300 mN [13]. Below 300°C, the films presented partial or total detachment at the a-C:H/a-SiC$_x$:H interface contributing to unfeasible application. The a-C:H/Si-containing interlayer/steel structures comprising interlayers formed by TEOS or HMDSO displayed similar delamination patterns below 300°C [14]. Similar structures formed with metallic interlayers (such as Ti and Cr) and diverse substrates usually feature DLC films with higher critical loads than nonmetallic interlayers. Maruno and Nishimoto [44] reported critical loads of DLC/Ti/Al films of 14.3 ± 1.0 N compared with the DLC/Al system with a critical load of 12.4 ± 1.2 N. Regarding Cr interlayers, Liu et al. [45] measured critical loads as high as (77 ± 2) N for the DLC/CrC/CrC$_x$/Cr/HSS multilayered system. Differently, the adhesion strength decreased to (18 ± 3) N for the DLC/Cr/HSS structure. PVD and HiPIMS are deposition processes that demand lower background pressures (~10^{-4} or 10^{-5} Pa) to produce DLC and metallic coatings. In comparison to PECVD, both PVD and

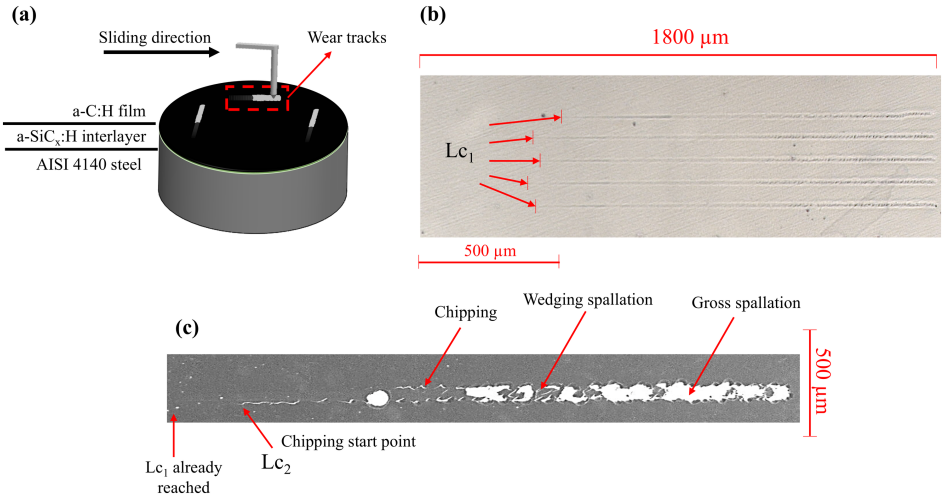

FIGURE 11 | Illustration of the (a) scratch test, (b) optical micrography, and (c) FEG-SEM of the wear track of the sample with the interlayer deposited at 175°C.

HiPIMS are more expensive and complex apparatuses. Hence, the industrial application of DLC thin films intermediated by metallic layers can have a cost–benefit factor impaired by the coating's high production cost.

Figure 11a displays an illustration of the scratch test, that is, the diamond tip sliding over the coating. Figure 11b,c shows the optical micrography of the nanoscratch trail and FEG-SEM micrography of the wear track of the sample with interlayer deposited at 175°C, respectively. The nanoscratch test enabled the determination of the parameter "Lc$_1$" whereas the scratch test allowed the measurement of "Lc$_2$." According to ASTM standard C1624-05 [46], "Lc$_1$" indicates the first cohesive cracking or failure in the coating (usually linked to chevron cracks), and "Lc$_2$" is related to coating-substrate adhesive failure at higher loads. Lc$_1$ is indicated in Figure 11b and Lc$_2$ in Figure 11c. Table 2 shows the Lc$_1$, Lc$_2$, and the failure modes and damage mechanisms for the coatings of the samples with different a-SiC$_x$:H deposition temperature. The data from other researches were added for comparison reasons.

The Lc$_1$ for the samples with interlayers deposited at 85°C, 125°C, 175°C, and 200°C was found within the nanoscratch applied load range (i.e., from 0 up to 500 mN). The samples with 100°C and 150°C exhibited Lc$_1$ higher than the maximum load of the nanoscratch test and lower than the minimum load of the scratch test. Therefore, these Lc$_1$ were simply identified as higher than 0.5 N.

From Figure 11c, one can see different damage mechanisms in the wear track of the sample with interlayer deposited at 175°C. Initially, there is a region with plastic deformation but without coating detachment. Then, one can observe the appearance of some chipping (Lc$_2$) followed by wedging and gross spallation. The wear tracks of the samples with the interlayers deposited at 85°C, 100°C, 125°C, 175°C, and 200°C displayed adhesion failure mainly in the form of wedging spallation (or compressive spallation). In this type of damage mechanism, the coating delaminates in order to decrease the elastic energy previously stored by the compressive stress applied by the Rockwell C type, as stated by Bull [50]. Differently from the others, the interlayer deposited at 150°C displayed a wear track with primary coating failure represented as gross spallation. This mechanism is caused by the poor adhesion coating-substrate and/or high residual stress in the films [50].

Kasiorowski et al. [47] investigated the effect of deposition techniques PECVD and PIID on the adhesion and damage mechanisms of DLC/Ti/TiN/TiC/AISI 4140 and DLC/SiC$_x$/AISI 4140, respectively. The steel substrate was quenched and tempered for both multilayered structures and not plasma nitrided. The researchers observed that gross spallation was the primary failure mode for the coatings deposited by PECVD (i.e., DLC and Ti/TiN/TiC). Lc$_1$, Lc$_2$, and Lc$_3$ were 8, 12, and 40 N, respectively. Lc$_1$ was associated with the appearance of lateral cracks on the DLC, while Lc$_2$ corresponded to the formation of conformal and buckling cracks on the Ti/TiN/TiC layers and Lc$_3$ to the delamination of the Ti/TiN/TiC layer. Differently from PECVD, the coatings deposited by PIID (i.e., DLC and SiC$_x$) showed wedging spallation as the primary adhesion failure mode. Lc$_1$ was 7 N (corresponded to chevron cracks), Lc$_2$ 9 N (related to the wedging spallation of the coatings), and Lc$_3$ 26 N. Both DLC and SiC$_x$ coatings were almost completely removed since Lc$_2$. The gross spallation of DLC deposited by PECVD was explained by its higher sp^3 hybridization and, therefore, hardness compared with the DLC deposited by PIID [47]. Siddiqui et al. [48] investigated a-C:H coatings deposited on X42Cr13/W precipitation hardened steels, intermediated by a-C:HW/WC/CrN layers. X42Cr13/W was not plasma nitrided. Scratch tests showed a Lc$_1$ of 13.6 N, corresponding to microcracks on the trail; Lc$_2$ of 19.8 N, related to buckling spallation/cohesive cracking of the coating; and Lc$_3$ of 40.4 N, characterized by the start of delamination of the coating from the substrate. Finally, Dalibon et al. [49] observed wedging spallation and Lc$_2$ of 12 N for DLC/Si interlayer/AISI 420 martensitic stainless-steel (not nitrided) structures.

Figure 12 contains the FEG-SEM image and chemical mapping by EDS demonstrating the adhesive failure of the coatings for the sample with a-SiC$_x$:H deposited at 175°C. One can observe that the critical failure occurred at the innermost

TABLE 2 | Lc_1, Lc_2, failure mode, and damage mechanisms for the a-C:H coatings of this work. Comparison with other researches.

Source	Configuration	a-SiC_x:H deposition temperature (°C)/ precursor	Deposition technique of the DLC and interlayer(s)	Lc_1 (N)	Lc_2 (N)	Damage mechanism(s)	Failure mode
This work	a-C:H/a-SiC_x:H/AISI 4140	85/TMS and Ar	PECVD	0.15 ± 0.006	4.3 ± 0.2	Wedging spallation	Adhesive
		100/TMS and Ar	PECVD	> 0.5	4.3 ± 0.2	Wedging spallation	Adhesive
		125/TMS and Ar	PECVD	0.23 ± 0.001	4.4 ± 0.4	Wedging spallation	Adhesive
		150/TMS and Ar	PECVD	> 0.5	4.2 ± 0.1	Gross spallation	Adhesive
		175/TMS and Ar	PECVD	0.11 ± 0.005	5.9 ± 0.4	Chipping, wedging spallation	Adhesive
		200/TMS and Ar	PECVD	0.15 ± 0.003	5.6 ± 0.8	Chipping, wedging spallation	Adhesive
Kasiorowski et al. [47]	DLC/Ti/TiN/TiC/AISI 4140 quenched and tempered, nonnitrided	Not informed/Ti metal target, Ar, Ar + N, and Ar + C_2H_2	PECVD	8	12	Gross spallation	Adhesive
	DLC/SiC_x/AISI 4140 quenched and tempered, nonnitrided	Not informed/TMS	PIID	7	9	Wedging spallation	Adhesive
Siddiqui et al. [48]	a-C:H/a-C:HW/WC/CrN/ X42Cr13/W nonnitrided	Not informed	PVD (CrN and WC), PECVD (a-C:H)	13.6	19.8	Buckling spallation	Cohesive
Dalibon et al. [49]	DLC/Si interlayer/AISI 420 martensitic stainless steel nonnitrided	Not informed/silane gas	PACVD	Not informed	12	Wedging spallation	Adhesive

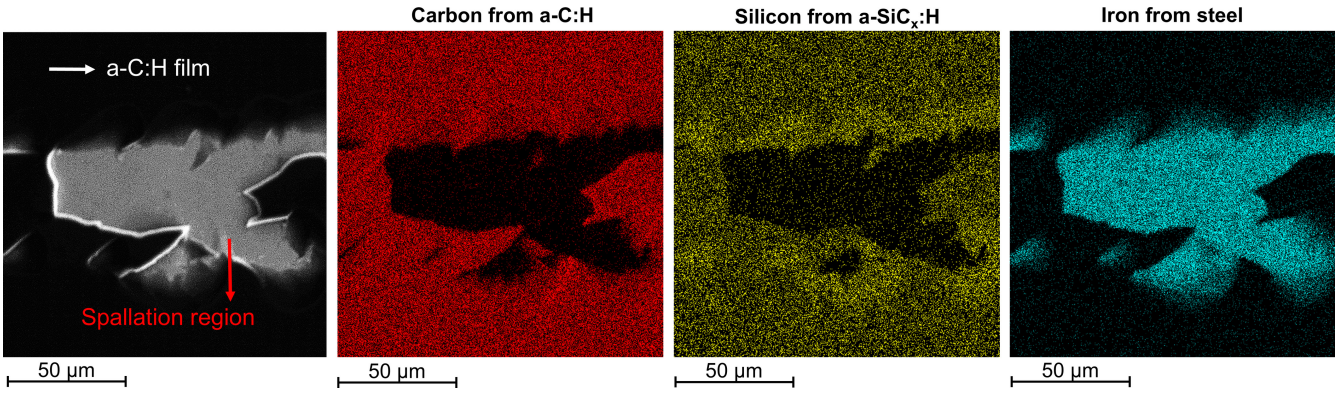

FIGURE 12 | FEG-SEM and chemical mapping by EDS of the a-C:H/a-SiC$_x$:H/steel structure's adhesive failure.

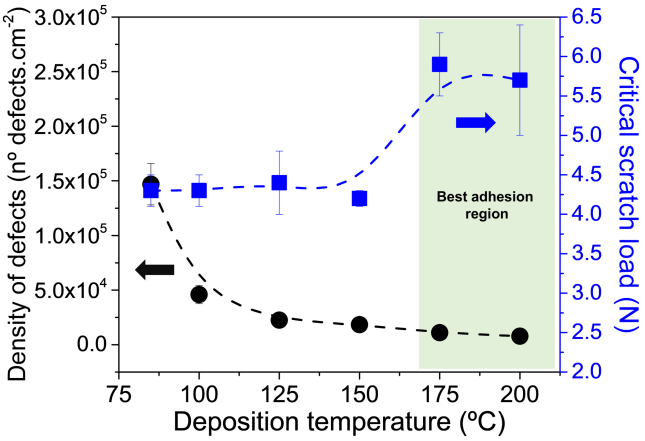

FIGURE 13 | Variation of the density of defects and critical scratch load with a-SiC$_x$:H deposition temperature.

interface (a-SiC$_x$:H/steel). All samples exhibited adhesive failure regardless of the deposition temperature. The interfaces are the regions with the highest failure possibility of the entire structure since they are composed of defects and dangling bonds [51]. The chemical mapping revealed a strong qualitative iron signal in the spallation region. Contrarily, the qualitative C and Si signals are weak in this region, which indicates their small presence in the respective wear track region. It is possible to associate the delamination at the a-SiC$_x$:H/steel interface with the oxygen content. Oxygen acts as a bond filler of dangling bonds and impairs interfacial adhesion. For comparison, the a-C:H/interlayer/steel structures with Si-containing interlayers deposited with HMDSO showed adhesive failure at the a-C:H/a-SiC$_x$:H interface [30]. With TMS and background pressure of 1.5 Pa, the coatings' adhesive failure followed two patterns: (1) the delamination at the a-C:H/a-SiC$_x$:H interface—when the interlayer was deposited at 300°C—and (2) the delamination at the a-SiC$_x$:H/steel interface—when the interlayer was deposited at 550°C [51].

The surface morphology of the a-C:H films was evaluated through the density of defects and roughness. For the image analysis (see Figure S2), defects were considered heterogeneities, such as pinholes (circular dark marks), voids (absence of coating), or particle nucleation in the a-C:H coatings. The evolution of roughness as a function of the interlayer deposition temperature is shown in Figure S3. Figure 13 shows the correlation between the density of defects, the critical scratch load, and the interlayer's deposition temperature. All a-C:H coatings presented a density of defects smaller than 1.5×10^5 defects.cm^{-2}. Despite the deposition temperature of the a-C:H film remaining constant at 80°C for all samples, it was possible to observe an influence of the deposition temperature of the Si-containing interlayer on the surface aspect of the coatings. When the temperature of the a-SiC$_x$:H interlayer increased, the density of defects exponentially decreased. This inverse phenomenon can be associated with the intensification of instabilities in the plasma region, detachment of already deposited products, effects of cathodic arcs, and/or unfinished chemical reactions that are potentialized at low deposition temperatures. For example, from 85°C to 100°C, there was a reduction of ~1.0×10^5 defects.cm^{-2} in the density of defects.

The presence of defects/heterogeneities in DLC coatings has been reported elsewhere [52, 53]. Yatsuzuka et al. [52] evaluated the presence of pinhole defects in DLC films prepared by a hybrid process of plasma-based ion implantation and deposition. The researchers observed an exponential decrease in the pinhole area ratio with the increase in film thickness (e.g., ~1.0×10^{-1}% for 0.5 µm to 3.0×10^{-6}% for 11 µm). The application of a Si-containing and C-containing interlayer between the DLC coating and the austenitic stainless-steel (SUS304) substrate considerably reduced the pinhole area ratio in the film (e.g., from 1.0×10^{-1}% for DLC/SUS304 to ~5.0×10^{-3}% for the DLC/interlayer/SUS304 system). Furthermore, Maerten et al. [53] observed microzones from 10 to 60 µm in DLC films. The defects can be characterized as pinholes and voids. The steel substrate was uncovered in some regions. In contact with a corrosive environment, the DLC coating would not be effective for corrosion protection in such regions.

An inverse behavior was observed between the density of defects and the film's critical scratch load when the interlayer's deposition temperature increased from 85°C up to 200°C (Figure 13). One can see that there has been an improvement in a-C:H overall adhesion with the homogenization of the coating's surface. The heterogeneities can act as points of weakness for both adhesion and corrosion resistance of a-C:H/a-SiC$_x$:H/steel structures. In addition, thinner films can be found due to a lower deposition rate, cathode arc effect, and/or gas detachment during the deposition process. It is interesting to correlate the

trend observed in Figure 13 with the one already commented on in Figure 10. The density of defects followed the same reduction trend with temperature as the one observed for the atomic percentage of oxygen at the outermost interface of the structure. This correlation points out that both chemical and surface features interfere with the adhesion of the coatings to the AISI 4140 steel substrate.

4 | Conclusion

In this paper, the physical–chemical, optical, morphological, and tribological properties of the a-C:H coatings were assessed. The hydrogenated DLC films were successfully deposited on AISI 4140 steel, intermediated by a hydrogenated amorphous silicon carbide interlayer at low deposition temperatures ($T \leq 200°C$). The critical scratch loads (Lc_2) ranged from ~4 to 6 N for all deposited conditions. The failure mode observed for all the samples was adhesive and the main damage mechanism was wedging spallation. It was observed that both physical–chemical and surface properties play an important role in the adhesion of a-C:H/a-SiC_x:H/AISI 4140 steel structure.

The optical absorption edge of the samples takes place in energies around 3.5 eV (or ~350 nm) and ~1.5 eV (or ~850 nm) for the a-SiC_x:H interlayer (mainly deposited at 150°C) and a-C:H film deposited for 60 min, respectively. From a physical–chemical point of view, the increase of oxygen contents at a-C:H/a-SiC_x:H or a-SiC_x:H/steel interface impairs the adhesion of the structure. Oxygen acts as a bond filler, preventing the formation of Si–C, C–C, and Si–Fe stronger bonds in these regions. The increase in the interlayer's deposition temperature contributed to the elimination of oxygen, which could be desorbed as $H_2O_{(g)}$, $CO_{2(g)}$, $SiO_{(g)}$, and $O_{2(g)}$ molecules. Furthermore, oxygen removal is easily enabled by lowering the background pressures inside the deposition reactor. The oxygen atoms are eliminated through sputtering (the collision of the ions impinging the interfaces surface will have higher energy). Comparing samples produced with 0.8 Pa (this work) as background pressure and 1.5 Pa [27] (both with a-SiC_x:H layer deposited at 100°C), the samples with 0.8 Pa exhibited five times less oxygen content than the samples with 1.5 Pa.

From a morphological point of view, the increase of the density of defects in the a-C:H coating weakened the adhesion of the a-C:H/a-SiC_x:H/steel structure. The density of defects followed the same reduction trend as the oxygen content with the increase of the interlayer's temperature. Defects, such as pinholes and voids, can negatively interfere with the adhesion of the structure as well as with the capacity for corrosion resistance of a-C:H thin films.

Furthermore, the use of a relatively high background pressure (i.e., 0.8 Pa), reached by mechanical pumping, combined with a lower a-SiC_x:H deposition temperature ($T \leq 200°C$) represents an advance in the industrial application field of a-C:H thin films. Such advance considers the deposition using a simple and low-cost PECVD system and the cut of expenses/time loss considering the decrease of the interlayer's deposition temperature.

Author Contributions

Vanessa Piroli: conceptualization, formal analysis, investigation, methodology, writing – original draft. **Michael Cristian Goldbeck:** writing – review and editing, formal analysis, investigation. **Jennifer Stefani Weber:** writing – review and editing, formal analysis, investigation. **Felipe Cemin:** writing – review and editing, formal analysis, investigation, writing – original draft. **Bruna Louise Perotti:** writing – review and editing, formal analysis, investigation. **Carla Daniela Boeira:** writing – review and editing, formal analysis, investigation. **Fernando Alvarez:** writing – review and editing, formal analysis. **Newton Kiyoshi Fukumasu:** writing – review and editing, formal analysis. **Antonio Ricardo Zanatta:** writing – review and editing, formal analysis, investigation, writing – original draft. **Alexandre Fassini Michels:** writing – review and editing, investigation, methodology. **Carlos Alejandro Figueroa:** writing – review and editing, supervision, resources, project administration, conceptualization.

Acknowledgments

The authors would like to thank the Epipolé Research Group colleagues for their support during this research and Mr. R. A. Barbieri for helping with FEG-SEM and EDS analysis in LCMIC-UCS. The Article Processing Charge for the publication of this research was funded by the Coordenação de Aperfeiçoamento de Pessoal de Nível Superior - Brasil (CAPES) (ROR identifier: 00x0ma614).

Funding

This work was supported by CAPES (#88887.475264/2020-00), INCT-INES (CNPq #465423/2014-0), and FAPERGS (#19/2551-0000656-0 and #19/2551-0002288-3) projects. V.P., M.C.G., J.S.W., F.C., B.L.P., C.D.B., N.K.F., F.A., A.R.Z, A.F.M., and C.A.F. are CNPq, CAPES, or FAPESP fellows.

Conflicts of Interest

The authors declare no conflicts of interest.

Data Availability Statement

The data that support the findings of this study are available in the Supporting Information of this article.

References

1. A. Grill, "Diamond-Like Carbon: State of the Art," *Diamond and Related Materials* 8 (1999): 428–434, https://doi.org/10.1016/s0925-9635(98)00262-3.

2. R. Zahid, M. B. H. Hassan, M. Varman, et al., "A Review on Effects of Lubricant Formulations on Tribological Performance and Boundary Lubrication Mechanisms of Non-Doped DLC/DLC Contacts," *Critical Reviews in Solid State and Materials Sciences* 42 (2017): 267–294, https://doi.org/10.1080/10408436.2016.1186599.

3. F. Černý, V. Jech, I. Štěpánek, A. Macková, and S. Konvičková, "Decorative a-C:H Coatings," *Applied Surface Science* 256 (2009): S77–S81, https://doi.org/10.1016/j.apsusc.2009.04.188.

4. D. K. Rajak, A. Kumar, A. Behera, and P. L. Menezes, "Diamond-Like Carbon (DLC) Coatings: Classification, Properties, and Applications," *Applied Sciences* 11 (2021): 4445, https://doi.org/10.3390/app11104445.

5. F. Cemin, L. T. Bim, C. M. Menezes, et al., "The Influence of Different Silicon Adhesion Interlayers on the Tribological Behavior of DLC Thin Films Deposited on Steel by EC-PECVD," *Surface and Coating Technology* 283 (2015): 115–121, https://doi.org/10.1016/j.surfcoat.2015.10.031.

6. P. Wang, X. Wang, T. Xu, W. Liu, and J. Zhang, "Comparing Internal Stress in Diamond-Like Carbon Films With Different Structure," *Thin Solid Films* 515 (2007): 6899–6903, https://doi.org/10.1016/j.tsf.2007.02.069.

7. S. Delfani-Abbariki, A. Abdollah-zadeh, S. M. M. Hadavi, M. Abedi, and S. M. R. Derakhshandeh, "Enhancing the Adhesion of Diamond-Like Carbon Films to Steel Substrates Using Silicon-Containing Interlayers," *Surface and Coating Technology* 350 (2018): 74–83, https://doi.org/10.1016/j.surfcoat.2018.06.055.

8. X. Sui, J. Liu, S. Zhang, J. Yang, and J. Hao, "Microstructure, Mechanical and Tribological Characterization of CrN/DLC/Cr-DLC Multilayer Coating With Improved Adhesive Wear Resistance," *Applied Surface Science* 439 (2018): 24–32, https://doi.org/10.1016/j.apsusc.2017.12.266.

9. Z. Huang, Z. Chen, W. Lang, and X. Wang, "Adhesion Studies of CrC/a-C:H Coatings Deposited With Anode Assisted Reactive Magnetron Sputtering Combined With DC-Pulsed Plasma Enhanced Chemical Vapor Deposition," *Materials* 14 (2021): 2954, https://doi.org/10.3390/ma14112954.

10. Y. J. Jo, T. F. Zhang, M. J. Son, and K. H. Kim, "Synthesis and Electrochemical Properties of Ti-Doped DLC Films by a Hybrid PVD/PECVD Process," *Applied Surface Science* 433 (2018): 1184–1191, https://doi.org/10.1016/j.apsusc.2017.10.151.

11. W. A. McMillan, "Bond Energies," in *Encyclopedia of Inorganic Chemistry*, ed. R. B. King (John Wiley & Sons, 2006), https://doi.org/10.1002/0470862106.id098.

12. J. Acker, K. Bohmhammel, G. J. K. Van den Berg, J. C. Van Miltenburg, and C. H. Kloc, "Thermodynamic Properties of Iron Silicides FeSi and α-$FeSi_2$," *Journal of Chemical Thermodynamics* 31 (1999): 1523–1536, https://doi.org/10.1006/jcht.1999.0550.

13. F. Cemin, L. T. Bim, C. M. Menezes, et al., "On the Hydrogenated Silicon Carbide (SiC_x:H) Interlayer Properties Prompting Adhesion of Hydrogenated Amorphous Carbon (a-C:H) Deposited on Steel," *Vacuum* 109 (2014): 180–183, https://doi.org/10.1016/j.vacuum.2014.07.015.

14. C. D. Boeira, L. M. Leidens, F. Cemin, et al., "A Comprehensive Study on Different Silicon-Containing Interlayers for a-C:H Adhesion on Ferrous Alloys," *Thin Solid Films* 645 (2018): 351–357, https://doi.org/10.1016/j.tsf.2017.10.043.

15. V. Piroli, J. S. Weber, M. C. Goldbeck, et al., "Well-Adhered Hydrogenated Amorphous Carbon Thin Films on Ferrous Alloy Using Silicon-Containing Interlayers at Low Temperatures," *Vacuum* 199 (2022): 110923, https://doi.org/10.1016/j.vacuum.2022.110923.

16. P. M. Martin, *Handbook of Deposition Technologies for Films and Coatings* (Elsevier, 2010).

17. C. D. Wagner, W. M. Riggs, L. E. Davis, J. F. Moulder, and G. E. Muilenberg, *Handbook of X-Ray Photoelectron Spectroscopy* (Perkin-Elmer Corporation, 1979).

18. G. Greczynski and L. Hultman, "X-Ray Photoelectron Spectroscopy: Towards Reliable Binding Energy Referencing," *Progress in Materials Science* 107 (2020): 100591, https://doi.org/10.1016/j.pmatsci.2019.100591.

19. G. Greczynski, R. Haasch, N. Hellgren, E. Lewin, and L. Hultman, "X-Ray Photoelectron Spectroscopy of Thin Films," *Nature Reviews Methods Primers* 3 (2023): 40, https://doi.org/10.1038/s43586-023-00225-y.

20. G. Greczynski and L. Hultman, "C 1s Peak of Adventitious Carbon Aligns to the Vacuum Level: Dire Consequences for Material's Bonding Assignment by Photoelectron Spectroscopy," *ChemPhysChem* 18 (2017): 1507–1512, https://doi.org/10.1002/cphc.201700126.

21. D. A. Shirley, "High-Resolution X-Ray Photoemission Spectrum of the Valence Bands of Gold," *Physical Review B* 5 (1972): 4709–4714, https://doi.org/10.1103/physrevb.5.4709.

22. C. D. Wagner, L. E. Davis, M. V. Zeller, J. A. Taylor, R. H. Raymond, and L. H. Gale, "Empirical Atomic Sensitivity Factors for Quantitative Analysis by Electron Spectroscopy for Chemical Analysis," *Surface and Interface Analysis* 3 (1981): 211–225, https://doi.org/10.1002/sia.740030506.

23. N. Abidi, *FTIR Microspectroscopy: Selected Emerging Applications* (Springer, 2021).

24. R. L. McCreery, *Raman Spectroscopy for Chemical Analysis* (John Wiley & Sons, 2000).

25. T. Nelis and R. Payling, *Glow Discharge Optical Emission Spectroscopy: A Practical Guide* (Royal Society of Chemistry, 2005).

26. M. A. Tamor and W. C. Vassell, "Raman "Fingerprinting" of Amorphous Carbon Films," *Journal of Applied Physics* 76 (1994): 3823–3830, https://doi.org/10.1063/1.357385.

27. F. Cemin, L. T. Bim, L. M. Leidens, et al., "Identification of the Chemical Bonding Prompting Adhesion of a-C:H Thin Films on Ferrous Alloy Intermediated by a SiC_x:H Buffer Layer," *ACS Applied Materials & Interfaces* 7 (2015): 15909–15917, https://doi.org/10.1021/acsami.5b03554.

28. V. Ţucureanu, A. Matei, and A. M. Avram, "FTIR Spectroscopy for Carbon Family Study," *Critical Reviews in Analytical Chemistry* 46 (2016): 502–520, https://doi.org/10.1080/10408347.2016.1157013.

29. W. Xie, A. Kawahito, T. Miura, et al., "Colorful Carbon Nanopopcorns Formed by Codepositing C_{60} With Diamond-Like Carbon Followed by Reaction With Water Vapor," *Chemistry Letters* 44 (2015): 1205–1207, https://doi.org/10.1246/cl.150470.

30. A. E. Crespi, L. M. Leidens, V. Antunes, et al., "Substrate Bias Voltage Tailoring the Interfacial Chemistry of a-SiC_x:H: A Surprising Improvement in Adhesion of a-C:H Thin Films Deposited on Ferrous Alloys Controlled by Oxygen," *ACS Applied Materials & Interfaces* 11 (2019): 18024–18033, https://doi.org/10.1021/acsami.9b03597.

31. R. Szeto and D. W. Hess, "Correlation of Chemical and Electrical Properties of Plasma-Deposited Tetramethylsilane Films," *Journal of Applied Physics* 52 (1981): 903–908, https://doi.org/10.1063/1.328774.

32. B. P. Swain and R. O. Dusane, "Effect of Substrate Temperature on HWCVD Deposited a-SiC:H Film," *Materials Letters* 61 (2007): 4731–4734, https://doi.org/10.1016/j.matlet.2007.03.029.

33. O. S. Heavens, "Optical Properties of Thin Films," *Reports on Progress in Physics* 23 (1960): 1–65, https://doi.org/10.1088/0034-4885/23/1/301.

34. F. S. Tehrani, M. Fakhredin, and M. J. Tafreshi, "The Optical Properties of Silicon Carbide Thin Films Prepared by HWCVD From Pure Silane and Methane Under Various Total Gas Partial Pressure," *Materials Research Express* 6 (2019): 086469, https://doi.org/10.1088/2053-1591/ab2843.

35. B. P. Swain, "The Analysis of Carbon Bonding Environment in HWCVD Deposited a-SiC:H Films by XPS and Raman Spectroscopy," *Surface and Coating Technology* 2021 (2006): 1589–1593, https://doi.org/10.1016/j.surfcoat.2006.02.029.

36. I. Barin, *Thermochemical Data of Pure Substances* (VCH, 1995).

37. S. D. Nehate, A. K. Saikumar, and K. B. Sundaram, "Influence of Substrate Temperature on Electrical and Optical Properties of Hydrogenated Boron Carbide Thin Films Deposited by RF Sputtering," *Coatings* 11 (2021): 1–9, https://doi.org/10.3390/coatings11020196.

38. J. Nishikawa, N. Sugihara, M. Nakano, J. Hieda, N. Ohtake, and H. Akasaka, "Effect of Si Incorporation on Corrosion Resistance of Hydrogenated Amorphous Carbon Film," *Diamond and Related Materials* 90 (2018): 207–213, https://doi.org/10.1016/j.diamond.2018.10.017.

39. F. Deku, S. Mohammed, A. Joshi-Imre, et al., "Effect of Oxidation on Intrinsic Residual Stress in Amorphous Silicon Carbide Films," *Journal*

of Biomedical Materials Research 107 (2019): 1654–1661, https://doi.org/10.1002/jbm.b.34258.

40. N. Liu, X. Huang, and J. J. Dubowski, "Selective Area In Situ Conversion of Si (0 0 1) Hydrophobic to Hydrophilic Surface by Excimer Laser Irradiation in Hydrogen Peroxide," *Journal of Physics D: Applied Physics* 47 (2014): 385106, https://doi.org/10.1088/0022-3727/47/38/385106.

41. M. Li, L. Jiang, Y. Sun, et al., "Correlation Study of Photoluminescence Properties and Mechanism of Hydrogenated Amorphous Silicon Carbide Films," *Journal of Luminescence* 212 (2019): 38–44, https://doi.org/10.1016/j.jlumin.2019.04.020.

42. S. Kwon, Y. Park, W. Ban, et al., "Effect of Plasma Power on Properties of Hydrogenated Amorphous Silicon Carbide Hardmask Films Deposited by PECVD," *Vacuum* 174 (2020): 109187, https://doi.org/10.1016/j.vacuum.2020.109187.

43. C. D. Boeira, L. M. Leidens, A. F. Michels, et al., "Influence of Base Pressure Prior to Deposition on the Adhesion Behaviour of Carbon Thin Films on Steel," *Applied Surface Science Advances* 2 (2020): 100034, https://doi.org/10.1016/j.apsadv.2020.100034.

44. H. Maruno and A. Nishimoto, "Adhesion and Durability of Multi-Interlayered Diamond-Like Carbon Films Deposited on Aluminum Alloy," *Surface and Coating Technology* 354 (2018): 134–144, https://doi.org/10.1016/j.surfcoat.2018.08.094.

45. L. Liu, Z. Wu, X. An, et al., "Excellent Adhered Thick Diamond-Like Carbon Coatings by Optimizing Hetero-Interfaces With Sequential Highly Energetic Cr and C Ion Treatment," *Journal of Alloys and Compounds* 735 (2018): 155–162, https://doi.org/10.1016/j.jallcom.2017.11.057.

46. ASTM Standard C1624-05, "Standard Test Method for Adhesion Strenght and Mechanical Failure Modes of Ceramic Coatings by Quantitative Single Point Scratch Testing," (2010), https://doi.org/10.1520/C1624-05.

47. T. Kasiorowski, J. Lin, P. Soares, et al., "Microstructural and Tribological Characterization of DLC Coatings Deposited by Plasma Enhanced Techniques on Steel Substrates," *Surface and Coating Technology* 389 (2020): 125615, https://doi.org/10.1016/j.surfcoat.2020.125615.

48. S. A. Siddiqui, G. Favaro, and M. B. Maros, "Investigation of the Damage Mechanism of CrN and Diamond-Like Carbon Coatings on Precipitation-Hardened and Duplex-Treated X42Cr13/W Tool Steel by 3D Scratch Testing," *Journal of Materials Engineering and Performance* 31 (2022): 7830–7842, https://doi.org/10.1007/s11665-022-06812-6.

49. E. L. Dalibon, J. N. Pecina, A. Cabo, V. J. Trava-Airoldi, and S. P. Brühl, "Fretting Wear Resistance of DLC Hard Coatings Deposited on Nitrided Martensitic Stainless Steel," *Journal of Materials Research and Technology* 8 (2019): 259–266, https://doi.org/10.1016/j.jmrt.2017.12.004.

50. S. J. Bull, "Failure Modes in Scratch Adhesion Testing," *Surface and Coating Technology* 50 (1991): 25–32, https://doi.org/10.1016/0257-8972(91)90188-3.

51. F. Cemin, C. D. Boeira, and C. A. Figueroa, "On the Understanding of the Silicon-Containing Adhesion Interlayer in DLC Deposited on Steel," *Tribology International* 94 (2016): 464–469, https://doi.org/10.1016/j.triboint.2015.09.044.

52. M. Yatsuzuka, J. Tateiwa, and H. Uchida, "Evaluation of Pinhole Defect in DLC Film Prepared by Hybrid Process of Plasma-Based Ion Implantation and Deposition," *Vacuum* 80 (2006): 1351–1355, https://doi.org/10.1016/j.vacuum.2006.01.069.

53. T. Maerten, C. Jaoul, R. Oltra, et al., "Micrometric Growth Defects of DLC Thin Films," *C-Journal of Carbon Research* 5 (2019): 73, https://doi.org/10.3390/c5040073.

Supporting Information

Additional supporting information can be found online in the Supporting Information section. **Figure S1:** Optical reflectance spectra of the samples with different a-SiC_x:H deposition temperatures and a-C:H deposition time of (a) 1 and (b) 60 min. **Figure S2:** Optical micrographs of the a-C:H thin films for samples with a-SiC_x:H deposited at 85°C and 175°C. Schematics of the defects' distribution in the structure. **Figure S3:** Variations of Ra and Rq parameters with a-SiC_x:H deposition temperature. The dashed lines are used to simplify the visualization. **Table S1:** a-SiC_x:H deposition temperature and a-SiC_x:H/steel interface's atomic content.